SIAM J. IMAGING SCIENCES
Vol. 3, No. 3, pp. 340–362

Reconstruction of Thin Tubular Inclusions in Three-Dimensional Domains Using Electrical Impedance Tomography*

Roland Griesmaier†

Abstract. We consider the inverse problem of reconstructing thin tubular inclusions inside a three-dimensional body from measurements of electrostatic currents and potentials on its boundary. By inclusions we mean objects with an electrical conductivity differing from that of the background material of the body. We apply an asymptotic expansion of the electrostatic potential on the boundary of the body as the thickness of the inclusions tends to zero to establish an asymptotic characterization of these inclusions in terms of the measurement data. This characterization is implemented in a noniterative reconstruction method similar to the factorization method for crack detection problems in two-dimensional domains. We present several numerical examples to illustrate our theoretical findings and to highlight the potentials and limitations of our method.

Key words. electrical impedance tomography, thin tubular inclusions, asymptotic expansions, factorization method

AMS subject classifications. 65N21, 35R30, 35C20

DOI. 10.1137/090764074

1. Introduction.

Electrical impedance tomography (EIT) is an imaging modality that recovers information on the conductivity distribution inside a body from electrostatic measurements on its boundary. This is a nonlinear severely ill-posed inverse problem (for review articles see, e.g., [7, 17]). Here, we consider a special case, supposing that a collection of thin tubular inclusions, i.e., objects covering thin tubular neighborhoods of certain sufficiently smooth curves, is embedded in a bounded three-dimensional body such that the conductivity inside the inclusions is significantly higher or lower than the background conductivity of the body, which we assume to be known. Our aim is to reconstruct these inclusions from measurements of the electrostatic potentials on the boundary of the body corresponding to all possible current flows through the same boundary. More precisely, we establish a method that reconstructs the location of curves inside the inclusions representing their positions, lengths, and shapes in the longitudinal direction. Potential applications are, e.g., the detection of shrinkage defects in castings in nondestructive testing or the reconstruction of buried wires or tubes in subsurface imaging.

The reconstruction method we propose is a variant of the factorization method originally developed by Kirsch [32] for an inverse scattering problem. Kirsch's method has been extended to inverse conductivity problems by Brühl and Hanke [9, 8], and corresponding methods for crack detection problems in two-dimensional domains have been established by Brühl, Hanke, and Pidcock [10] and by Kirsch and Ritter [34]. Due to its sound theoretical foundation and

*Received by the editors July 7, 2009; accepted for publication (in revised form) May 19, 2010; published electronically July 22, 2010.
http://www.siam.org/journals/siims/3-3/76407.html
†Department of Mathematical Sciences, University of Delaware, Newark, DE 19716 (griesmai@math.udel.edu).

its numerical efficiency, the factorization method has been widely studied and extended to various inverse problems in recent years (see, e.g., [3, 12, 23, 24, 26, 27, 28, 29, 30, 36, 37, 41] for contributions related to EIT). An excellent introduction to this subject can be found in the monograph [33] by Kirsch and Grinberg.

Since in contrast to the two-dimensional case curves in three-dimensional domains do not support well-defined boundary conditions, the mathematical justification of the factorization method for crack detection problems from [10, 34] cannot be carried over to our inverse problem straightforwardly. Rather we follow Brühl, Hanke, and Vogelius [11] and study the asymptotic behavior of the difference of the electrostatic potentials on the boundary of the body in the presence and in the absence of the inclusions as the thickness of the inclusions tends to zero, i.e., as the inclusions shrink to curves. Applying results of Capdeboscq and Vogelius [13, 14, 15], we find that the leading order term in the corresponding asymptotic expansion of this difference has a singularity along these curves. We use this to develop a binary criterion to decide whether or not an arbitrary given curve inside the body belongs to such an infinitesimal inclusion. This criterion is then implemented in a noniterative reconstruction algorithm, which can be seen as a natural generalization of the factorization method for crack detection problems in two-dimensional domains from [10, 34] to our setting.

Reconstruction methods for thin tubular inclusions, different from our approach but also based on asymptotic expansions of the boundary potential as the thickness of the inclusions tends to zero, have, e.g., been studied for two-dimensional domains in [1, 2, 38, 40] and recently for thin straight cylindrical inclusions in three-dimensional domains by Beretta et al. [6].

This article is organized as follows. After describing the mathematical model for the forward problem in the next section, we summarize some results of the asymptotic analysis from [13, 14, 15] and apply them to our setup. Then, in section 3 we use these results to develop the theoretical foundation of our reconstruction method, establishing an asymptotic characterization of the position and shape of infinitesimally thin tubular inclusions in terms of the measurement data. This is done first for a single inclusion to simplify the notation, while the general case of multiple inclusions is discussed in the appendix. We formulate the reconstruction algorithm in section 4, and in section 5 we comment on its numerical implementation. There we also provide numerical results based on simulated forward data to demonstrate the performance of our reconstruction method.

2. The mathematical setting.

Suppose $\Omega \subset \mathbb{R}^3$ is a bounded domain with smooth boundary $\partial\Omega$ and denote by ν the unit outward normal to $\partial\Omega$. We consider a smooth conductivity distribution $\gamma_0 \in C^\infty(\Omega)$ such that $0 < c_0 \le \gamma_0 \le C_0 < \infty$ in Ω for some constants c_0 and C_0. Prescribing a *boundary current*

$$f \in L^2_\diamond(\partial\Omega) := \left\{ f \in L^2(\partial\Omega) \;\middle|\; \int_{\partial\Omega} f \, \mathrm{d}s = 0 \right\}$$

at $\partial\Omega$, the induced *electrostatic potential* u_0 in Ω satisfies the boundary value problem

$$\nabla \cdot (\gamma_0 \nabla u_0) = 0 \qquad \text{in } \Omega, \tag{2.1a}$$

$$\gamma_0 \frac{\partial u_0}{\partial \nu} = f \qquad \text{on } \partial\Omega. \tag{2.1b}$$

We choose u_0 to be the unique solution of these equations in

$$H^1_\diamond(\Omega) := \left\{ u \in H^1(\Omega) \;\middle|\; \int_{\partial\Omega} u \, \mathrm{d}s = 0 \right\};$$

i.e., its trace $u_0|_{\partial\Omega}$ belongs to $L^2_\diamond(\partial\Omega)$. Throughout we call γ_0 the *background conductivity* and u_0 the *background potential*.

Next, let $K \subset \Omega$ be a simple (i.e., non-self-intersecting but possibly closed) curve in Ω with a C^3 parameterization by arc-length $p_K : [0, L] \to \Omega$ such that K is separated away from the boundary $\partial\Omega$; i.e., $\operatorname{dist}(K, \partial\Omega) \geq 2d_0$ for some constant $d_0 > 0$. Assuming that $p'_K(s) \times p''_K(s) \neq 0$ for all $s \in [0, L]$, the *Frenet–Serret frame* $(\boldsymbol{t}_K, \boldsymbol{n}_K, \boldsymbol{b}_K)$ for K is defined by $\boldsymbol{t}_K(p_K(s)) := p'_K(s)$, $\boldsymbol{n}_K(p_K(s)) := p''_K(s)/|p''_K(s)|$, and $\boldsymbol{b}_K(p_K(s)) := \boldsymbol{t}_K(p_K(s)) \times \boldsymbol{n}_K(p_K(s))$ for $s \in [0, L]$. We consider the *normal bundle* of K in $\mathbb{R}^3$,

$$E_K := \{(x, v) \in K \times \mathbb{R}^3 \mid \boldsymbol{t}_K(x) \cdot v = 0\},$$

and the *exponential map* $\exp : E_K \to \mathbb{R}^3$ given by $\exp(x, v) := x + v$. Denoting by

$$E_{K,r} := \{(x, v) \in E_K \mid |v| < r\}$$

the associated *open disk bundle* of radius $r > 0$, the tubular neighborhood theorem (cf., e.g., Spivak [42, Thm. 20, p. 467]) yields that the restriction of exp to $E_{K,r}$ is a C^1 diffeomorphism from $E_{K,r}$ to a *tubular neighborhood* $U_{K,r} \subset \{x \in \Omega \mid \operatorname{dist}(x, K) < r\}$ of $K \setminus \{p_K(0), p_K(L)\}$ if r is sufficiently small. The critical radius, i.e., the supremum over all r such that $\exp : E_{K,r} \to U_{K,r}$ is a diffeomorphism, is called *injectivity radius* $R(K)$ of K (see Litherland et al. [39] for a detailed analysis of $R(K)$). So, assuming that $r < R(K)$, we can henceforth identify $E_{K,r}$ with $U_{K,r}$.

Let $B \subset U_{K,r}$ be a bounded domain containing $K \setminus \{p_K(0), p_K(L)\}$ in its interior such that $p_K(0), p_K(L) \in \partial B$ and $\operatorname{dist}(B, \partial\Omega) \geq d_0$, and consider the family of bounded domains

$$\omega_\varepsilon := \{(x, \varepsilon v) \in E_{K,r} \mid x + v \in B\}, \qquad 0 < \varepsilon \leq 1. \tag{2.2}$$

Note that $\omega_1 = B$ and that ω_ε shrinks to the curve K as $\varepsilon \to 0$. Each ω_ε, $0 < \varepsilon \leq 1$, is considered as a *(thin) tubular inclusion* contained in Ω causing a conductivity distribution of the form

$$\gamma_\varepsilon(x) := \begin{cases} \gamma_1(x), & x \in \omega_\varepsilon, \\ \gamma_0(x), & x \in \Omega \setminus \overline{\omega_\varepsilon}, \end{cases} \tag{2.3}$$

where $\gamma_1 \in C^\infty(\Omega)$ is such that $0 < c_1 \leq \gamma_1 \leq C_1 < \infty$ in Ω for some constants c_1 and C_1 and the conductivity γ_ε is significantly smaller or larger than the background conductivity γ_0 on K; i.e.,

$$\gamma_1 + \alpha < \gamma_0 \quad \text{or} \quad \gamma_0 < \gamma_1 + \alpha \qquad \text{on } K \text{ for some constant } \alpha > 0. \tag{2.4}$$

The electrostatic potential u_ε in the presence of such an inclusion ω_ε is the solution of the Neumann problem

$$\nabla \cdot (\gamma_\varepsilon \nabla u_\varepsilon) = 0 \qquad \text{in } \Omega, \tag{2.5a}$$

$$\gamma_\varepsilon \frac{\partial u_\varepsilon}{\partial \nu} = f \qquad \text{on } \partial\Omega \tag{2.5b}$$

in $H^1_\diamond(\Omega)$ (using the same normalization as for u_0).

Therewith we introduce the *Neumann-to-Dirichlet operators* Λ_0 and Λ_ε from $L^2_\diamond(\partial\Omega)$ to $L^2_\diamond(\partial\Omega)$, which map boundary currents f on the corresponding boundary potentials $u_0|_{\partial\Omega}$ and $u_\varepsilon|_{\partial\Omega}$, respectively. These operators are well known to be compact and self-adjoint (see, e.g., [8]). The inverse problem we consider in this work asks us to reconstruct the position, length, and shape in the longitudinal direction of a thin tubular inclusion ω_ε as in (2.2) for one particular $\varepsilon > 0$ small enough from given data $\Lambda_\varepsilon - \Lambda_0$. In practice this means that sufficiently accurate finite dimensional realizations of Λ_ε and Λ_0 have to be known in order to compute a reliable approximation of $\Lambda_\varepsilon - \Lambda_0$. While the approximation of Λ_ε is supposed to be obtained from measurements of boundary potentials $u_\varepsilon|_{\partial\Omega}$ corresponding to a linearly independent collection of boundary currents f, the approximation for Λ_0 can be simulated numerically, recalling our assumption that the background conductivity γ_0 is known.

To develop a reconstruction method for this inverse problem, we first study the asymptotic behavior of $\Lambda_\varepsilon - \Lambda_0$ as the parameter ε tends to zero, i.e., as ω_ε shrinks to K. Using the Frenet–Serret frame $(\boldsymbol{t}_K, \boldsymbol{n}_K, \boldsymbol{b}_K)$, the parameterization p_K of K can be extended to a diffeomorphism $P_K : [0, L] \times \tilde{B}_r(0) \to U_{K,r}$,

$$(s, \xi) \mapsto p_K(s) + \xi_1 \boldsymbol{n}_K(p_K(s)) + \xi_2 \boldsymbol{b}_K(p_K(s)),$$

where $\tilde{B}_r(0)$ denotes the ball of radius r around the origin $(0, 0)$ in $\mathbb{R}^2$ and $\xi = (\xi_1, \xi_2)$. Substituting $\hat{\xi} := \xi/\varepsilon$, we obtain that

$$\begin{aligned}
\frac{|\omega_\varepsilon|}{\varepsilon^2} &= \frac{1}{\varepsilon^2} \int_{\omega_\varepsilon} 1 \, \mathrm{d}x = \frac{1}{\varepsilon^2} \int_{U_{\varepsilon r}} \chi_{\omega_\varepsilon}(x) \, \mathrm{d}x \\
&= \frac{1}{\varepsilon^2} \int_0^L \int_{\tilde{B}_{\varepsilon r}(0)} \chi_{\omega_\varepsilon}(P_K(l, \xi)) |\det(DP_K)|(l, \xi) \, \mathrm{d}\xi \, \mathrm{d}l \\
&= \int_0^L \int_{\tilde{B}_r(0)} \chi_B(P_K(l, \hat{\xi})) |\det(DP_K)|(l, \varepsilon\hat{\xi}) \, \mathrm{d}\hat{\xi} \, \mathrm{d}l,
\end{aligned}$$

where $\chi_{\omega_\varepsilon}$ (resp., χ_B) denotes the characteristic function for ω_ε (resp., B) and $|\omega_\varepsilon|$ is the Lebesgue measure of ω_ε. Defining $h_0 \in L^\infty(K)$ by

$$h_0(p_K(l)) := \int_{\tilde{B}_r(0)} \chi_B(P_K(l, \hat{\xi})) |\det(DP_K)|(l, 0) \, \mathrm{d}\hat{\xi}, \qquad l \in [0, L], \tag{2.6}$$

we find that

$$\lim_{\varepsilon \to 0} \frac{|\omega_\varepsilon|}{\varepsilon^2} = \int_0^L h_0(p_K(l)) \, \mathrm{d}l = \int_K h_0(x) \, \mathrm{d}s(x).$$

Furthermore, for any $\phi \in C(\overline{\Omega})$,

$$\begin{aligned}
\frac{1}{|\omega_\varepsilon|} \int_{\omega_\varepsilon} \phi(x) \, \mathrm{d}x &= \frac{1}{|\omega_\varepsilon|} \int_{U_{\varepsilon r}} \chi_{\omega_\varepsilon}(x) \phi(x) \, \mathrm{d}x \\
&= \frac{1}{|\omega_\varepsilon|} \int_0^L \int_{\tilde{B}_{\varepsilon r}} \chi_{\omega_\varepsilon}(P_K(l, \xi)) \phi(P_K(l, \xi)) |\det(DP_K)|(l, \xi) \, \mathrm{d}\xi \, \mathrm{d}l \\
&= \frac{\varepsilon^2}{|\omega_\varepsilon|} \int_0^L \int_{\tilde{B}_r} \chi_B(P_K(l, \hat{\xi})) \phi(P_K(l, \varepsilon\hat{\xi})) |\det(DP_K)|(l, \varepsilon\hat{\xi}) \, \mathrm{d}\hat{\xi} \, \mathrm{d}l.
\end{aligned}$$

Thus,

$$\lim_{\varepsilon\to 0}\frac{1}{|\omega_\varepsilon|}\int_{\omega_\varepsilon}\phi(x)\,\mathrm{d}x=\frac{1}{\int_K h_0(x)\,\mathrm{d}s(x)}\int_K \phi(x)h_0(x)\,\mathrm{d}s(x). \tag{2.7}$$

The right-hand side of this equation determines the weak* limit of the regular Borel measures $(|\omega_\varepsilon|^{-1}\chi_{\omega_\varepsilon}\,\mathrm{d}x)_{\varepsilon>0}$ as $\varepsilon\to 0$ in the dual space of $C(\overline{\Omega})$.

Combining this result with Theorem 1 from [13], we can give a precise description of the asymptotic behavior of $(u_\varepsilon-u_0)|_{\partial\Omega}$ on the boundary of Ω. Before we state this result in Theorem 2.1, we introduce the Neumann function N for the differential operator $\nabla\cdot\gamma_0\nabla$ in Ω as the distributional solution of

$$\begin{aligned}\nabla_x\cdot(\gamma_0(x)\nabla_x N(x,y))&=-\delta_y(x), && x\in\Omega,\\ \gamma_0(x)\frac{\partial N(x,y)}{\partial\nu(x)}&=-\frac{1}{|\partial\Omega|}, && x\in\partial\Omega,\end{aligned}$$

with the normalization $\int_{\partial\Omega}N(x,\cdot)\,\mathrm{d}s(x)=0$. It is well known that N is symmetric in its arguments in $(\Omega\times\Omega)\setminus\mathrm{diag}(\Omega\times\Omega)$, i.e., $N(x,y)=N(y,x)$ for $x\neq y$, and that N can be extended by continuity to $(\overline{\Omega}\times\Omega\cup\Omega\times\overline{\Omega})\setminus\mathrm{diag}(\Omega\times\Omega)$. Note also that $\int_{\partial\Omega}N(x,y)f(y)\,\mathrm{d}s(y)=u_0(x)$ for $x\in\Omega$.

Theorem 2.1 (cf. Capdeboscq and Vogelius [13, Thm. 1]). *Assume $K\subset\Omega$ is a simple C^3 curve satisfying $\mathrm{dist}(K,\partial\Omega)\geq 2d_0$ for some constant $d_0>0$. Let $(\varepsilon_n)_{n\in\mathbb{N}}$ be a sequence in $]0,1]$ converging to zero and consider accordingly a sequence $(\omega_{\varepsilon_n})_{n\in\mathbb{N}}$ of subsets of Ω as defined in (2.2). Denote by $N(x,y)$ the Neumann function for the differential operator $\nabla\cdot\gamma_0\nabla$ in the domain Ω, and let u_0 and u_{ε_n} be the solutions of (2.1) and (2.5) corresponding to the boundary values $f\in L^2_\diamond(\partial\Omega)$, respectively. Then there exist a subsequence, also denoted by $(\omega_{\varepsilon_n})_{n\in\mathbb{N}}$, and a matrix valued function $\mathbb{M}\in L^2(K;\mathbb{R}^{3\times 3})$, called a* polarization tensor, *such that*

$$(u_{\varepsilon_n}-u_0)(y)={\varepsilon_n}^2\int_K(\gamma_0-\gamma_1)(x)\nabla_x N(x,y)\cdot\mathbb{M}(x)\nabla u_0(x)h_0(x)\,\mathrm{d}s(x)+o({\varepsilon_n}^2)$$

for $y\in\partial\Omega$. The function $\mathbb{M}$ is independent of f and satisfies

$$\mathbb{M}^\top(x)=\mathbb{M}(x), \tag{2.8}$$

$$\min\left\{1,\frac{\gamma_0(x)}{\gamma_1(x)}\right\}|\xi|^2\leq\xi^\top\mathbb{M}(x)\xi\leq\max\left\{1,\frac{\gamma_0(x)}{\gamma_1(x)}\right\}|\xi|^2\qquad\text{for all }\xi\in\mathbb{R}^3 \tag{2.9}$$

and a.e. $x\in K$. The term $o({\varepsilon_n}^2)$ is such that $\|o({\varepsilon_n}^2)\|_{L^\infty(\partial\Omega)}/{\varepsilon_n}^2$ converges to 0 as $n\to\infty$ for $f\in L^2_\diamond(\partial\Omega)$, uniformly on $\{f\in L^2_\diamond(\partial\Omega)\mid\|f\|_{L^2(\partial\Omega)}\leq 1\}$.

Remark 2.2 (polarization tensor). The polarization tensor $\mathbb{M}$ can be described as a weak* limit as follows. Let $(\varepsilon_n)_{n\in\mathbb{N}}$ be the sequence introduced in the beginning of Theorem 2.1 and consider for $n\in\mathbb{N}$ and $1\leq j\leq 3$ the solution $v^j_{\varepsilon_n}\in H^1_\diamond(\Omega)$ of the boundary value problem

$$\begin{aligned}\nabla\cdot(\gamma_{\varepsilon_n}\nabla v^j_{\varepsilon_n})&=\nabla\cdot(\gamma_0 e_j) && \text{in }\Omega,\\ \gamma_{\varepsilon_n}\frac{\partial v^j_{\varepsilon_n}}{\partial\nu}&=\gamma_0\nu_j && \text{on }\partial\Omega,\end{aligned}$$

where (e_1, e_2, e_3) denotes the standard basis of $\mathbb{R}^3$ and ν_j is the jth component of the unit outward normal to $\partial\Omega$. In [13] it is shown that $(1/|\omega_{\varepsilon_n}|)\chi_{\omega_{\varepsilon_n}}\nabla v^j_{\varepsilon_n}$, $1 \le j \le 3$, is bounded in $L^1(\Omega)$ (uniformly with respect to ε_n), which is then used to prove that there exists a subsequence (the subsequence mentioned in Theorem 2.1), also denoted by $(\omega_{\varepsilon_n})_{n\in\mathbb{N}}$, such that for any $\phi \in C(\overline{\Omega})$,

$$\int_K \phi(x)\mathbb{M}_{ij}(x)\widetilde{h_0}(x)\,\mathrm{d}s(x) = \lim_{n\to\infty}\frac{1}{|\omega_{\varepsilon_n}|}\int_{\omega_{\varepsilon_n}} \phi(x)\frac{\partial v^j_{\varepsilon_n}}{\partial x_i}(x)\,\mathrm{d}x,$$

where $\widetilde{h_0} := (1/\int_K h_0\,\mathrm{d}s)h_0$. Therefore, $\mathbb{M}$ is a generalization of the classical polarization tensor as described, e.g., in [4, 19]. For the special case of thin cylindrical inclusions, i.e., when K is a straight line and the cross-section $B \cap E_{K,r}(x)$ of B is the same for all $x \in K$, where $E_{K,r}(x)$ denotes fiber of the bundle $E_{K,r}$ over $x \in K$, a more explicit description of $\mathbb{M}$ has recently been established in [6].

Our analysis in the following sections does not rely on the actual form of the polarization tensor but only on its properties (2.8) and (2.9), which are independent of the particular subsequence $(\omega_{\varepsilon_n})_{n\in\mathbb{N}}$. The reconstruction algorithm essentially determines the support of the limiting measure from (2.7).

3. Asymptotic characterization of the inclusions.

Henceforth we consider a subsequence $(\omega_{\varepsilon_n})_{n\in\mathbb{N}}$ as in Theorem 2.1 such that the actual inclusion ω_ε corresponds to one element in this sequence, and we denote by $\mathbb{M}$ the corresponding polarization tensor. Introducing the operator $T : L^2_\diamond(\partial\Omega) \to L^2_\diamond(\partial\Omega)$,

$$Tf := \int_K (\gamma_0 - \gamma_1)(x)\nabla_x N(x,\,\cdot\,)\cdot\mathbb{M}(x)\nabla u_0(x)\widetilde{h_0}(x)\,\mathrm{d}s(x), \tag{3.1}$$

where as before u_0 denotes the background potential corresponding to the boundary current f, we obtain from Theorem 2.1 that

$$\Lambda_{\varepsilon_n} - \Lambda_0 = \varepsilon_n^2 T + o(\varepsilon_n^2) \tag{3.2}$$

in $\mathcal{L}(L^2_\diamond(\partial\Omega), L^2_\diamond(\partial\Omega))$, i.e., in the space of bounded linear operators from $L^2_\diamond(\partial\Omega)$ onto itself.

3.1. Factorization of T.

For small values of ε_n, the $o(\varepsilon_n^2)$ term in (3.2) is dominated by the first term on the right-hand side of this equation. So, if the difference $\Lambda_{\varepsilon_n} - \Lambda_0$ is perturbed, e.g., by measurement errors, typically only information contained in the *leading order term* T is available to recover the inclusions. To analyze T we introduce two auxiliary maps, the integral operator $L : L^2(K;\mathbb{R}^3) \to L^2_\diamond(\partial\Omega)$,

$$L\psi := \int_K \psi(x)\cdot\nabla_x N(x,\,\cdot\,)\,\mathrm{d}s(x), \tag{3.3}$$

and the multiplication operator $F : L^2(K;\mathbb{R}^3) \to L^2(K;\mathbb{R}^3)$,

$$F\phi := (\gamma_0 - \gamma_1)h_0\mathbb{M}\phi. \tag{3.4}$$

Since the kernel of L is smooth, L is a compact operator. Furthermore, using standard properties of positive definite symmetric matrices, (2.8) and (2.9) yield that $\|\mathbb{M}\|_{L^\infty(K;\mathbb{R}^{3\times 3})}$ is bounded and thus F is a bounded linear operator. We conclude from (2.8) that F is self-adjoint, and from (2.4), (2.6), and (2.9) we find that F is coercive if $\gamma_1|_K < \gamma_0|_K$, i.e., there exists a constant $c_F > 0$ such that

$$\langle \phi, F\phi \rangle_{L^2(K;\mathbb{R}^3)} \geq c_F \|\phi\|^2_{L^2(K;\mathbb{R}^3)} \qquad \text{for all } \phi \in L^2(K;\mathbb{R}^3),$$

and that $-F$ is coercive if $\gamma_1|_K > \gamma_0|_K$. For $\psi \in L^2(K;\mathbb{R}^3)$ and $f \in L^2(\partial\Omega)$ changing the order of integration gives

$$\begin{aligned}\langle L\psi, f\rangle_{L^2(\partial\Omega)} &= \int_{\partial\Omega}\left(\int_K \psi(x)\cdot\nabla_x N(x,y)\,\mathrm{d}s(x)\right) f(y)\,\mathrm{d}s(y)\\ &= \int_K \psi(x)\cdot\nabla_x\left(\int_{\partial\Omega} N(x,y) f(y)\,\mathrm{d}s(y)\right)\mathrm{d}s(x)\\ &= \langle \psi, \nabla u_0|_K\rangle_{L^2(K;\mathbb{R}^3)}.\end{aligned}$$

Therefore, the transpose $L^\top : L^2_\diamond(\partial\Omega) \to L^2(K;\mathbb{R}^3)$ of L is given by

$$L^\top f = \nabla u_0|_K. \tag{3.5}$$

Note that the trace $u_0|_K$ is well defined since the background potential is smooth in the interior of Ω.

Lemma 3.1. (a) *The leading order term T in the asymptotic expansion (3.2) admits the factorization*

$$T = LFL^\top. \tag{3.6}$$

(b) *The range of L and the range of $|T|^{1/2}$ coincide; i.e., $\mathcal{R}(L) = \mathcal{R}(|T|^{1/2})$.*

Proof. Part (a) follows directly by comparing (3.3), (3.4), and (3.5) with (3.1). Part (b) is a consequence of the properties of L and F mentioned before which allow for applying [33, Cor. 1.22, p. 23]. ∎

3.2. Range of L. In the next section we use the range identity from Lemma 3.1(b) to reconstruct the position, length, and shape in the longitudinal direction of the inclusion ω_ε from $\Lambda_\varepsilon - \Lambda_0$. To that end we analyze in the following the range of the operator L in detail.

Let $\Sigma \subset \Omega$ be a second simple curve in Ω with a C^3 parameterization by arc-length $p_\Sigma : [0,l] \to \Omega$, and denote by $\boldsymbol{t}_\Sigma(p_\Sigma(s)) := p'_\Sigma(s)$ the unit tangent vector to Σ at $p_\Sigma(s)$. For $\varphi \in C^1(\Sigma;\mathbb{R}^3)$ such that

$$|\varphi(x)| - |\boldsymbol{t}_\Sigma(x)\cdot\varphi(x)| \neq 0 \qquad \text{for all } x \in \Sigma, \tag{3.7}$$

let

$$w_{\Sigma,\varphi} := \int_\Sigma \varphi(x)\cdot\nabla_x N(x,\,\cdot\,)\,\mathrm{d}s(x) \qquad \text{and} \qquad g_{\Sigma,\varphi} := w_{\Sigma,\varphi}|_{\partial\Omega}. \tag{3.8}$$

Note that, for instance, choosing $v_0 \in E_\Sigma(p_\Sigma(0))$, where E_Σ denotes the normal bundle of Σ, and assuming that Σ is short enough with respect to its curvature such that $|v_0| - |\boldsymbol{t}_\Sigma(x) \cdot v_0| \neq 0$ for all $x \in \Sigma$, we can use $\varphi \equiv v_0$.

Proposition 3.2. *Let $\Sigma \subset \Omega$ be a simple C^3 curve, let $\varphi \in C^1(\Sigma; \mathbb{R}^3)$ satisfying (3.7), and let $g_{\Sigma,\varphi} \in L^2_\diamond(\partial\Omega)$ as in (3.8). Then, $g_{\Sigma,\varphi} \in \mathcal{R}(L) = \mathcal{R}(|T|^{1/2})$ if and only if $\Sigma \subset K$.*

Proof. First assume that $\Sigma \subset K$. Then φ can be extended to a function $\tilde{\varphi} \in L^2(K; \mathbb{R}^3)$ by

$$\tilde{\varphi}(x) := \begin{cases} \varphi(x), & x \in \Sigma, \\ 0, & x \in K \setminus \Sigma. \end{cases}$$

Thus, recalling (3.3) and Lemma 3.1(b), it follows that $g_{\Sigma,\varphi} \in \mathcal{R}(L) = \mathcal{R}(|T|^{1/2})$.

On the other hand, if $g_{\Sigma,\varphi} \in \mathcal{R}(L) = \mathcal{R}(|T|^{1/2})$, then

$$g_{\Sigma,\varphi} = \int_K \psi(x) \cdot \nabla_x N(x, \cdot)\, \mathrm{d}s(x) \qquad \text{for some } \psi \in L^2(\Sigma; \mathbb{R}^3).$$

Therefore, both

$$v_1 := \int_K \psi(x) \cdot \nabla_x N(x, \cdot)\, \mathrm{d}s(x) \quad \text{and} \quad v_2 := \int_\Sigma \varphi(x) \cdot \nabla_x N(x, \cdot)\, \mathrm{d}s(x)$$

solve the Cauchy problem

$$\nabla \cdot (\gamma_0 \nabla w) = 0 \quad \text{in } \Omega \setminus (K \cup \Sigma), \qquad \frac{\partial w}{\partial \nu}\Big|_{\partial\Omega} = 0, \quad w|_{\partial\Omega} = g_{\Sigma,\varphi}. \tag{3.9}$$

Uniqueness of solutions to (3.9) (see Dautray and Lions [20, Cor. 11, p. 262]) yields that $v_1 = v_2$ in $\Omega \setminus (K \cup \Sigma)$.

Now we assume that $\Sigma \not\subset K$ and show that v_2 is unbounded close to Σ, which contradicts $v_1 = v_2$ in $\Omega \setminus (K \cup \Sigma)$, since v_1 is smooth away from K. The proof is based on a variation of the arguments used in the proof of the jump relations for double layer potentials by Kress [35, pp. 80–81] and in the proof of the uniqueness result [6, Prop. 4.1]. Let $z \in \Sigma \setminus K$ such that z is not an endpoint of Σ, decompose $\varphi = \varphi_t + \varphi_n$, where $\varphi_t := (\varphi \cdot \boldsymbol{t}_\Sigma)\boldsymbol{t}_\Sigma$ and $\varphi_n := \varphi - \varphi_t$, and consider a straight line $\Gamma := \{z + ta \mid 0 < t \leq \tau\}$, where $a := \varphi_n(z)/|\varphi_n(z)|$. The constant $\tau > 0$ is such that $\Gamma \subset \Omega \setminus K$, and we denote by $B_r(z)$ a ball of radius $r > 0$ (small enough) around z (see Figure 1 for a sketch).

Following Friedman and Vogelius [22], the Neumann function can be written for each $y \in \Omega$ as

$$N(\,\cdot\,, y) = \frac{1}{\gamma_0(y)} \Phi(\,\cdot\,, y) + R_N(\,\cdot\,, y),$$

where $\Phi(x, y) := 1/(4\pi|x - y|)$ denotes the fundamental solution of the Laplace equation and $R_N(\,\cdot\,, y)$ solves

$$\begin{aligned} \nabla_x \cdot (\gamma_0(x) \nabla_x R_N(x, y)) &= -\frac{1}{4\pi\gamma_0(y)} \frac{\nabla\gamma_0(x) \cdot (x - y)}{|x - y|^3}, && x \in \Omega, \\ \gamma_0(x) \frac{\partial R_N(x, y)}{\partial \nu(x)} &= -\frac{1}{|\partial\Omega|} + \frac{\gamma_0(x)}{4\pi\gamma_0(y)} \frac{(x - y) \cdot \nu(x)}{|x - y|^3}, && x \in \partial\Omega. \end{aligned}$$

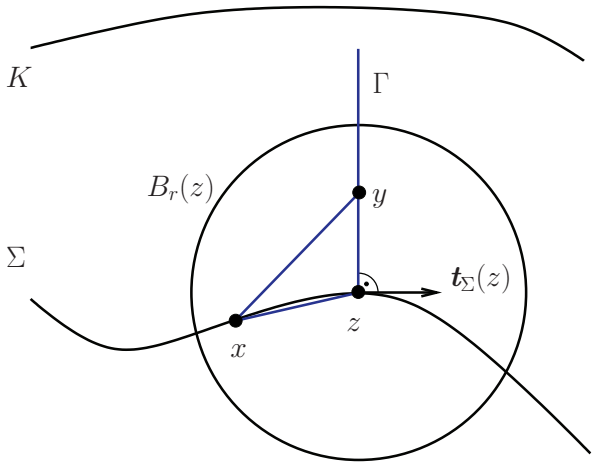

Figure 1. *Sketch of the geometry.*

As mentioned in [22], observing that the function $x \mapsto \frac{\nabla\gamma_0(x)\cdot(x-y)}{|x-y|^3}$ is in $L^p(\Omega)$ for $1 \le p < 3/2$ and the right-hand side is uniformly bounded in this space for $y \in \Gamma$, it follows that $R_N(\,\cdot\,, y) \in W^{2,p}(\Omega)$ and $\|R_N(\,\cdot\,, y)\|_{W^{2,p}(\Omega)}$ is uniformly bounded for $y \in \Gamma$.

We write

$$v_2 = \frac{1}{\gamma_0}\left(v_{2,t} + v_{2,n} + \gamma_0 \int_\Sigma \varphi(x) \cdot \nabla_x R_N(x, \,\cdot\,)\, \mathrm{d}s(x)\right), \tag{3.10}$$

where

$$v_{2,t} := \int_\Sigma \varphi_t(x) \cdot \nabla_x \Phi(x, \,\cdot\,)\, \mathrm{d}s(x) \quad \text{and} \quad v_{2,n} := \int_\Sigma \varphi_n(x) \cdot \nabla_x \Phi(x, \,\cdot\,)\, \mathrm{d}s(x),$$

and observe that due to the regularity of $R_N(\,\cdot\,, y)$, the last term in (3.10) is bounded by $(\max_{x\in\Sigma} |\varphi(x)|)\|R_N(\,\cdot\,, y)\|_{W^{2,1}(\Omega)}$, i.e., uniformly for $y \in \Gamma$.

Using integration by parts, we find that for $y = z + ta \in \Gamma$, $t > 0$,

$$v_{2,t}(y) = (\varphi \cdot \boldsymbol{t}_\Sigma)(p_\Sigma(l))\Phi(p_\Sigma(l), y) - (\varphi \cdot \boldsymbol{t}_\Sigma)(p_\Sigma(0))\Phi(p_\Sigma(0), y) - \widetilde{v_{2,t}}(y),$$

where $\widetilde{v_{2,t}}(y) := \int_\Sigma \frac{\partial(\boldsymbol{t}_\Sigma\cdot\varphi)}{\partial \boldsymbol{t}_\Sigma}(x)\Phi(x, y)\, \mathrm{d}s(x)$. Furthermore,

$$\begin{aligned}
\widetilde{v_{2,t}}(y) &= \int_{\Sigma\setminus B_r(z)} \frac{\partial(\boldsymbol{t}_\Sigma \cdot \varphi)}{\partial \boldsymbol{t}_\Sigma}(x)\Phi(x, y)\, \mathrm{d}s(x) + \frac{\partial(\boldsymbol{t}_\Sigma \cdot \varphi)}{\partial \boldsymbol{t}_\Sigma}(z) \int_{\Sigma\cap B_r(z)} \Phi(x, y)\, \mathrm{d}s(x) \\
&\quad + \int_{\Sigma\cap B_r(z)} \left(\frac{\partial(\boldsymbol{t}_\Sigma \cdot \varphi)}{\partial \boldsymbol{t}_\Sigma}(x) - \frac{\partial(\boldsymbol{t}_\Sigma \cdot \varphi)}{\partial \boldsymbol{t}_\Sigma}(z)\right)\Phi(x, y)\, \mathrm{d}s(x) \\
&=: I_1(y) + I_2(y) + I_3(y).
\end{aligned}$$

Observing that for $x \in \Sigma \setminus B_r(z)$, $|x - y| = |x - z - ta| \ge |x - z| - t \ge r - t \ge r/2$ if $t \le r/2$, we obtain that $|I_1(y)| \le C/r$. Here and for the rest of this proof $C > 0$ denotes a generic constant the value of which might be different at different occurrences.

Since $\boldsymbol{t}_\Sigma$ is continuous on Σ, we can assume that r is small enough such that $\boldsymbol{t}_\Sigma(x)\cdot\boldsymbol{t}_\Sigma(z)\geq 1/2$ in $\Sigma\cap B_r(z)$ and that this set is connected. Then $\Sigma\cap B_r(z)$ can be projected bijectively on the tangent line to Σ at z, and we can estimate

$$\begin{aligned}|I_2(y)| &= \left|\frac{\partial(\boldsymbol{t}_\Sigma\cdot\varphi)}{\partial\boldsymbol{t}_\Sigma}(z)\int_{\Sigma\cap B_r(z)}\Phi(x,y)\,\mathrm{d}s(x)\right|\\ &\leq C\left|\frac{\partial(\boldsymbol{t}_\Sigma\cdot\varphi)}{\partial\boldsymbol{t}_\Sigma}(z)\right|\left|2\int_0^r\frac{1}{4\pi(\rho^2+t^2)^{1/2}}\,\mathrm{d}\rho\right|\\ &\leq C\left|\frac{\partial(\boldsymbol{t}_\Sigma\cdot\varphi)}{\partial\boldsymbol{t}_\Sigma}(z)\right|\left|\log(r+\sqrt{r^2+t^2})-\log(t)\right|.\end{aligned}$$

To estimate $|I_3(y)|$ we recall that Σ is C^3 and that φ is continuously differentiable. Thus, we find from Taylor's theorem that

$$|\boldsymbol{t}_\Sigma(x)-\boldsymbol{t}_\Sigma(z)|\leq C|x-z|\qquad\text{and}\qquad|\nabla(\boldsymbol{t}_\Sigma\cdot\varphi)(x)-\nabla(\boldsymbol{t}_\Sigma\cdot\varphi)(z)|\leq C|x-z|.$$

Therefore,

$$\left|\frac{\partial(\boldsymbol{t}_\Sigma\cdot\varphi)}{\partial\boldsymbol{t}_\Sigma}(x)-\frac{\partial(\boldsymbol{t}_\Sigma\cdot\varphi)}{\partial\boldsymbol{t}_\Sigma}(z)\right|\leq C|x-z|,$$

and

$$|I_3(y)|\leq C\int_{\Sigma\cap B_r(z)}\frac{|x-z|}{4\pi|x-y|}\,\mathrm{d}s(x)\leq Cr.$$

Next we consider $v_{2,n}$ from (3.10) and decompose it as

$$\begin{aligned}v_{2,n}(y) &= \int_{\Sigma\setminus B_r(z)}\varphi_n(x)\cdot\nabla_x\Phi(x,y)\,\mathrm{d}s(x)+|\varphi_n(z)|\int_{\Sigma\cap B_r(z)}\frac{\varphi_n(x)}{|\varphi_n(x)|}\cdot\nabla_x\Phi(x,y)\,\mathrm{d}s(x)\\ &\quad+\int_{\Sigma\cap B_r(z)}\big(|\varphi_n(x)|-|\varphi_n(z)|\big)\frac{\varphi_n(x)}{|\varphi_n(x)|}\cdot\nabla_x\Phi(x,y)\,\mathrm{d}s(x)\\ &=: I_4(y)+I_5(y)+I_6(y).\end{aligned}$$

Analogous to the estimate for $|I_1(y)|$, we find that $|I_4(y)|\leq C/r^2$.

To estimate $I_5(y)$, we observe that

$$\begin{aligned}|I_5(y)| &\geq |\varphi_n(z)|\left|\int_{\Sigma\cap B_r(z)}\frac{\varphi_n(z)}{|\varphi_n(z)|}\cdot\nabla_x\Phi(x,y)\,\mathrm{d}s(x)\right|\\ &\quad-|\varphi_n(z)|\left|\int_{\Sigma\cap B_r(z)}\left(\frac{\varphi_n(x)}{|\varphi_n(x)|}-\frac{\varphi_n(z)}{|\varphi_n(z)|}\right)\cdot\nabla_x\Phi(x,y)\,\mathrm{d}s(x)\right|,\end{aligned}$$

and applying Taylor's formula, we find for the second term on the right-hand side that

$$\begin{aligned}\left|\int_{\Sigma\cap B_r(z)}\left(\frac{\varphi_n(x)}{|\varphi_n(x)|}-\frac{\varphi_n(z)}{|\varphi_n(z)|}\right)\cdot\nabla_x\Phi(x,y)\,\mathrm{d}s(x)\right| &\leq C\int_{\Sigma\cap B_r(z)}\frac{|x-z||x-y|}{4\pi|x-y|^3}\,\mathrm{d}s(x)\\ &\leq C2\int_0^r\frac{\rho}{\rho^2+t^2}\,\mathrm{d}\rho\leq C\big(-\log(t)+\log(r^2+t^2)\big).\end{aligned}$$

Recalling that $a := \varphi_n(z)/|\varphi_n(z)|$, we get for the other term that

$$\begin{aligned}\left|\int_{\Sigma\cap B_r(z)} \frac{\varphi_n(z)}{|\varphi_n(z)|}\cdot\nabla_x\Phi(x,y)\,\mathrm{d}s(x)\right| &= \left|\int_{\Sigma\cap B_r(z)} \frac{x-z-ta}{4\pi|x-z-ta|^3}\,\mathrm{d}s(x)\right| \\ &= \left|\int_{\Sigma\cap B_r(z)} \left(\frac{t}{4\pi|x-z-ta|^3} - \frac{a\cdot(x-z)}{4\pi|x-z-ta|^3}\right)\mathrm{d}s(x)\right| \\ &\geq \int_{\Sigma\cap B_r(z)} \left(\frac{t}{4\pi|x-z-ta|^3} - \frac{|a\cdot(x-z)|}{4\pi|x-z-ta|^3}\right)\mathrm{d}s(x).\end{aligned}$$

Using Taylor's formula (as done, e.g., in [35, p. 79]), it follows that $|a\cdot(x-z)| \leq C|x-z|^2$. Therefore, arguing as in the derivation of the estimate of $|I_2(y)|$ and projecting on the tangent line for Σ at z, we find that

$$\begin{aligned}&\left|\int_{\Sigma\cap B_r(z)} \frac{\varphi_n(z)}{|\varphi_n(z)|}\cdot\nabla_x\Phi(x,y)\,\mathrm{d}s(x)\right| \\ &\qquad\geq C\left(2\int_0^r \frac{t}{4\pi(\rho^2+t^2)^{3/2}}\,\mathrm{d}\rho - 2\int_0^r \frac{c\rho^2}{4\pi(\rho^2+t^2)^{3/2}}\,\mathrm{d}\rho\right) \\ &\qquad\geq C\left(\frac{r}{t\sqrt{r^2+t^2}} - \left(-\frac{r}{\sqrt{r^2+t^2}} + \log(r+\sqrt{r^2+t^2}) - \log(t)\right)\right).\end{aligned}$$

Finally, using the estimates

$$\left|\frac{\varphi(x)}{|\varphi(x)|}\cdot(x-y)\right| = \left|\frac{\varphi(x)}{|\varphi(x)|}\cdot(x-z+ta)\right| \leq C(|x-z|^2+t)$$

and $|\varphi_n(x)-\varphi_n(z)| \leq C|x-z|$, which both follow from Taylor's theorem, we obtain that

$$|I_6(y)| \leq C\int_{\Sigma\cap B_r(z)} \frac{|x-z|(|x-z|^2+t)}{4\pi|x-y|^3}\,\mathrm{d}s(x) \leq C2\int_0^r \frac{\rho(\rho^2+t)}{(\rho^2+t^2)^{3/2}}\,\mathrm{d}\rho \leq C.$$

So, letting t tend to zero, we obtain that $I_1(y) = I_3(y) = I_4(y) = I_6(y) = \mathcal{O}(1)$, $I_2(y) = \mathcal{O}(\log(t^{-1}))$, and $|I_5(y(t))| \geq Ct^{-1}$ if $|\varphi_n(z)| \neq 0$. Therefore, recalling (3.7), $v_2(z+ta)$ is unbounded as $t \to 0$. Hence, $\Sigma \subset K$, which ends the proof. ∎

4. Reconstruction of the inclusions. The range criterion from Proposition 3.2 yields a preliminary noniterative method for reconstructing the curve K from the leading order term T: Covering Ω with a sufficiently large set of *test curves* $\Sigma \subset \Omega$ and choosing density functions $\varphi \in C^1(\Sigma;\mathbb{C}^3)$ satisfying (3.7), we could check for each pair (Σ,φ) whether or not the corresponding *test function* $g_{\Sigma,\varphi}$ is contained in $\mathcal{R}(|T|^{1/2})$ and so decide whether $\Sigma \subset K$. In this section we extend this idea and develop a numerical algorithm to reconstruct the position, length, and shape in the longitudinal direction of the inclusion ω_ε from the given data $\Lambda_\varepsilon - \Lambda_0$.

For this purpose we first consider the spectral decomposition of the operator $|T|$,

$$|T|f = \sum_{i=0}^{\infty} \lambda_i \langle v_i, f\rangle_{L^2(\partial\Omega)} v_i, \qquad f \in L^2_\diamond(\partial\Omega),$$

where $(\lambda_i)_{i\in\mathbb{N}}$ are the eigenvalues of $|T|$ written in nonincreasing order according to their multiplicity and $(v_i)_{i\in\mathbb{N}}$ are the corresponding eigenvectors. The Picard criterion from functional analysis (cf., e.g., [35, p. 279]) implies that

$$g_{\Sigma,\varphi} \in \mathcal{R}(|T|^{1/2}) \quad \Longleftrightarrow \quad g_{\Sigma,\varphi} \perp \mathcal{N}(T) \qquad \text{and} \qquad \sum_{i=0}^{\infty} \frac{\langle g_{\Sigma,\varphi}, v_i\rangle^2_{L^2(\partial\Omega)}}{\lambda_i} < \infty. \tag{4.1}$$

Note that in contrast to $\Lambda_\varepsilon - \Lambda_0$ the operator T might not be injective. Observing that L from (3.3) is injective, which can be seen using arguments similar to those employed in the proof of Proposition 3.2, the injectivity of the operator F from (3.4) and the factorization (3.6) yield that $\mathcal{N}(T) = \mathcal{N}(L^\top)$. This means that $\mathcal{N}(T)$ consists of all boundary currents $f \in L^2_\diamond(\partial\Omega)$ such that the gradient of the corresponding background potential u_0 from (2.1) vanishes on the (unknown) curve K. (If, for instance, $\gamma_0 \equiv 1$, one can choose f such that $u_0 = x_1^2 - x_2^2 - (1/|\partial\Omega|)\int_{\partial\Omega}(x_1^2 - x_2^2)\,\mathrm{d}s(x)$. Then u_0 is harmonic and its gradient $\nabla u_0 = (2x_1, -2x_2, 0)^\top$ vanishes on the straight line $\mathbb{R}e_3$.) Nevertheless, we ignore in the following the orthogonality condition in (4.1). This could lead to false-positive results in the reconstruction method, but we never observed such effects in our numerical tests.

Recalling that the actual inclusion ω_ε is assumed to be an element of the sequence $(\omega_{\varepsilon_n})_{n\in\mathbb{N}}$ as considered in Theorem 2.1, we approximate in the following the Picard sum in (4.1) using the given data $\Lambda_\varepsilon - \Lambda_0$. To this end we introduce the spectral decomposition of $|\Lambda_{\varepsilon_n} - \Lambda_0|$, $n \in \mathbb{N}$, by

$$|\Lambda_{\varepsilon_n} - \Lambda_0| f = \sum_{i=0}^{\infty} \lambda_{\varepsilon_n,i} \langle v_{\varepsilon_n,i}, f\rangle_{L^2(\partial\Omega)} v_{\varepsilon_n,i}, \qquad f \in L^2_\diamond(\partial\Omega),$$

where $(\lambda_{\varepsilon_n,i})_{i\in\mathbb{N}}$ are the eigenvalues of $|\Lambda_{\varepsilon_n} - \Lambda_0|$ written in nonincreasing order according to their multiplicity and $(v_{\varepsilon_n,i})_{i\in\mathbb{N}}$ are the corresponding eigenvectors. Recalling (3.2), perturbation theory for linear operators shows that the eigenvalues of $|T|$ and $|\Lambda_{\varepsilon_n} - \Lambda_0|$ fulfill

$$\lambda_{\varepsilon_n,i} = \varepsilon_n^2 \lambda_i + o(\varepsilon_n^2) \qquad \text{for } i \in \mathbb{N} \text{ as } n \to \infty \tag{4.2}$$

and that (assuming appropriate choices of multiple eigenvectors) the orthogonal projections

$$P_{\varepsilon_n,i} : L^2_\diamond(\partial\Omega) \to \operatorname{span}_{\mathbb{R}}\{v_{\varepsilon_n,i}\} \qquad \text{and} \qquad P_i : L^2_\diamond(\partial\Omega) \to \operatorname{span}_{\mathbb{R}}\{v_i\},$$

$i \in \mathbb{N}$, on the corresponding eigenspaces satisfy

$$P_{\varepsilon_n,i} = P_i + o(1) \qquad \text{for } i \in \mathbb{N} \text{ as } n \to \infty$$

(see, e.g., [25, pp. 83–84], Lechleiter [36], or Kato [31]). So, denoting the eigenvalues, eigenvectors, and projections corresponding to the given data $\Lambda_\varepsilon - \Lambda_0$ by $(\lambda_{\varepsilon,i})_{i\in\mathbb{N}}$, $(v_{\varepsilon,i})_{i\in\mathbb{N}}$, and $(P_{\varepsilon,i})_{i\in\mathbb{N}}$, respectively, we substitute $P_i \approx P_{\varepsilon,i}$ and $\lambda_i \approx \lambda_{\varepsilon,i}/\varepsilon^2$ in (4.1) to obtain

$$\sum_{i=0}^{N} \frac{\langle g_{\Sigma,\varphi}, v_i\rangle^2_{L^2(\partial\Omega)}}{\lambda_i} \approx \varepsilon^2 \sum_{i=0}^{N} \frac{\langle g_{\Sigma,\varphi}, v_{\varepsilon,i}\rangle^2_{L^2(\partial\Omega)}}{\lambda_{\varepsilon,i}} \tag{4.3}$$

for any $N \in \mathbb{N}$.

Next, instead of sampling the domain Ω using a large setof test curves Σ, we follow [10, 34] and consider a rectangular equidistant *sampling grid* Ω_h in Ω. For each *test point* $z \in \Omega_h$ we introduce a *test dipole*

$$g_{z,d} := d \cdot \nabla_z N(z, \cdot)\big|_{\partial\Omega}, \tag{4.4}$$

with (constant) polarization $d \in \mathbb{R}^3$ of length 1. Note that $g_{z,d}$ can be viewed as the limit of some test function $g_{\Sigma,\varphi}$ from (3.8) with an appropriate test curve Σ (containing z) and the density function $\varphi \equiv d \in C^1(\Sigma;\mathbb{R}^3)$, as Σ shrinks to the point z. For $N \in \mathbb{N}$ large enough, $z \in \Omega_h$, and a unit vector $d \in \mathbb{R}^3$, we define the normalized Picard sum

$$W(z,d) := \sum_{i=0}^{N} \frac{\langle g_{z,d}, v_{\varepsilon,i}\rangle^2_{L^2(\partial\Omega)}}{\lambda_{\varepsilon,i}} \Big/ \sum_{i=0}^{N} \langle g_{z,d}, v_{\varepsilon,i}\rangle^2_{L^2(\partial\Omega)}. \tag{4.5}$$

According to (4.1), (4.3), and Proposition 3.2, we expect $1/W(z,d)$ to be large for points z close to the inclusion ω_ε and polarizations d that are not tangential to its base curve K around z (cf. (3.7)). So, visualizations of $1/W(z,d)$ on Ω_h for appropriate polarizations d can be used to estimate the position, length, and shape in the longitudinal direction of the thin tubular inclusion ω_ε. As outlined in the appendix, the same is true for multiple inclusions.

5. Numerical examples. For the numerical results presented in this section we consider a simplified test problem assuming that $\Omega = B_1(0)$ is the unit ball in $\mathbb{R}^3$ centered at the origin and that the conductivities $\gamma_0 \equiv 1$ and $\gamma_1 \equiv \kappa$ are constant with $\kappa \in]0,1[\cup]1,\infty[$, and therefore γ_ε from (2.3) is piecewise constant. However, the reconstruction algorithm can be implemented for arbitrary domains and conductivity distributions as introduced in section 2 as well.

5.1. Numerical simulation of $\Lambda_\varepsilon - \Lambda_0$. To obtain a finite dimensional realization of $\Lambda_\varepsilon - \Lambda_0$, we consider a linearly independent set of boundary currents, simulate the difference in the corresponding boundary potentials $(u_\varepsilon - u_0)|_{\partial\Omega}$, expand these data in an appropriate basis, and store the corresponding coefficients in a matrix. For our particular example this can be done as outlined in the following. Introducing spherical coordinates (r,θ,ϕ) such that a generic point $x \in \Omega$ is characterized by $x = r\sin(\theta)\cos(\phi)e_1 + r\sin(\theta)\sin(\phi)e_2 + r\cos(\theta)e_3$ with $r \geq 0$, $\theta \in [0,\pi]$ and $\phi \in [0,2\pi]$, we consider (real valued) *spherical harmonics*

$$Y_l^m(\theta,\phi) := \begin{cases} C_l^m P_l^m(\cos(\theta))\cos(m\phi), & 0 \leq m \leq l, \\ C_l^{|m|} P_l^{|m|}(\cos(\theta))\sin(|m|\phi), & -l \leq m \leq -1, \end{cases}$$

$l \geq 1$, where

$$C_l^m := \begin{cases} \sqrt{\frac{2l+1}{4\pi}}, & m = 0, \\ (-1)^m \sqrt{\frac{2l+1}{2\pi}\frac{(l-m)!}{(l+m)!}}, & 1 \leq m \leq l, \end{cases}$$

and P_l^m (resp., $P_l^{|m|}$) are the associated Legendre functions (see, e.g., Colton and Kress [18, p. 24]). The functions Y_l^m, $-l \leq m \leq l$ and $l \geq 1$, form a complete orthonormal system in $L^2_\diamond(\partial\Omega)$, and choosing boundary currents $f = Y_l^m$, $-l \leq m \leq l$ and $l \geq 1$, the corresponding background potentials solving (2.1) are given by

$$u_0(r,\theta,\phi) = \frac{1}{l} r^l Y_l^m(\theta,\phi) \qquad \text{in } \Omega.$$

So, observing that the difference $v := u_\varepsilon - u_0$ of solutions to (2.1) and (2.5) corresponding to the same boundary current f solves

$$\begin{aligned} \nabla \cdot (\gamma_\varepsilon \nabla v) &= \nabla \cdot ((\gamma_\varepsilon - 1)\nabla u_0) && \text{in } \Omega, \\ \frac{\partial v}{\partial \nu} &= 0 && \text{on } \partial\Omega \end{aligned}$$

in $H^1_\diamond(\Omega)$, we simulate $\Lambda_\varepsilon - \Lambda_0$ by computing v for the boundary currents $f = Y_l^m$, $-l \le m \le l$ and $1 \le l \le 8$. We use the finite element software FEMLAB to solve these forward problems, interpolate the Dirichlet boundary values of the solutions on an equiangular grid on $\partial\Omega$, and expand the result in spherical harmonics Y_l^m, $-l \le m \le l$ and $1 \le l \le 8$. Collecting the resulting coefficients for all boundary currents in a matrix $M \in \mathbb{R}^{80\times 80}$ column by column yields a finite dimensional approximation of the operator $\Lambda_\varepsilon - \Lambda_0$. To estimate the numerical error contained in this approximation, we can compute the nonsymmetric part of M,

$$\delta_M := \|M - M^\top\|_2. \tag{5.1}$$

Since $\Lambda_\varepsilon - \Lambda_0$ is self-adjoint, this should be zero for exact data and of order of the data error otherwise.

The singular value decomposition

$$Ma = \sum_{i=1}^{80} \tilde\sigma_i (\tilde v_i \cdot a)\tilde u_i, \qquad a \in \mathbb{R}^{80}, \tag{5.2}$$

with singular values $(\tilde\sigma_i)_{i=1}^{80}$ written in nonincreasing order according to their multiplicity and singular vectors $(\tilde u_i)_{i=1}^{80}$ and $(\tilde v_i)_{i=1}^{80}$, gives approximations of the eigenvalues and eigenvectors of $|\Lambda_\varepsilon - \Lambda_0|$. The error of these approximations of the eigenvalues is of the same order as δ_M.

Example 5.1 (asymptotic behavior of the eigenvalues of $\Lambda_\varepsilon - \Lambda_0$). To illustrate the asymptotic behavior of the eigenvalues of $\Lambda_\varepsilon - \Lambda_0$ as $\varepsilon \to 0$ (cf. (4.2)) we consider a cylindrical inclusion ω_ε of radius ε and length 1 centered at the origin such that its axis of symmetry is aligned with the vector $(1, 1, 1)$. To facilitate the numerical solution of the forward problem, we avoid edges in the geometry by attaching two hemispheres of radius ε to the ends of this cylinder. A visualization of this setup with $\varepsilon = 0.01$ can be found in Figure 3 (left). The large sphere in this plot corresponds to the boundary of the ball Ω, and to enhance the three-dimensional perspective we included the orthogonal projections of the inclusion ω_ε on the coordinate planes. The conductivity inside ω_ε is given by $\kappa = 0.5$. Figure 2 shows approximations of the first 30 eigenvalues of $|\Lambda_\varepsilon - \Lambda_0|$ for $\varepsilon = 0.1$, $\varepsilon = 0.1/\sqrt{10} \approx 0.0316$, and $\varepsilon = 0.01$. The gray shaded area indicates the error bound from (5.1). According to (4.2) we expect the eigenvalues to behave essentially like ε^2, which is indeed the case for the first 12 eigenvalues. The other eigenvalues decay slightly faster. This suggests that the approximation (4.3) is applicable at least for moderate values of N in this example.

Since the leading order term T in the asymptotic expansion (3.2) is of infinite rank, there is no gap that distinguishes the range (resp., essential range) and the nullspace (resp., noise subspace) of T (resp., $\Lambda_\varepsilon - \Lambda_0$)) in these plots. In fact, recalling the characterization of the kernel of T mentioned in section 4, the finite dimensional approximation $(1/\varepsilon^2)M$ of

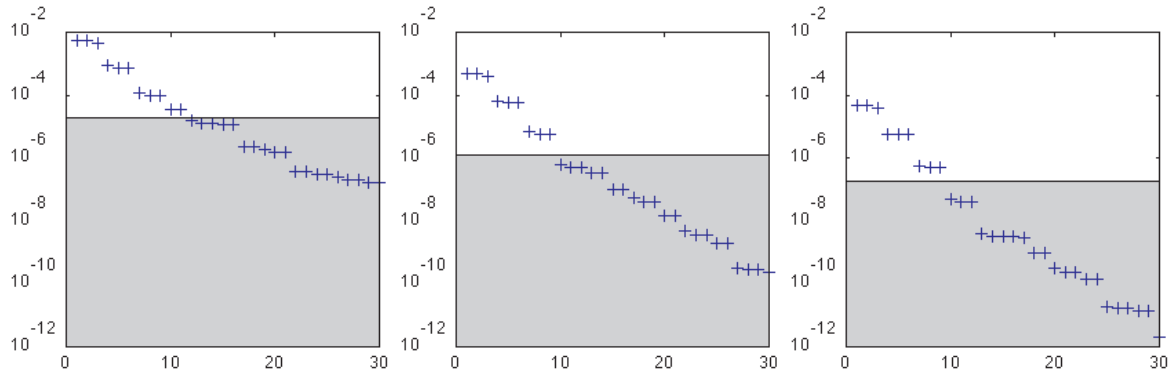

Figure 2. *Eigenvalues of* $\Lambda_\varepsilon - \Lambda_0$ *from Example 5.1 for* $\varepsilon = 0.1$, $\varepsilon = 0.0316$, *and* $\varepsilon = 0.001$ *(from left to right).*

$(1/\varepsilon^2)(\Lambda_\varepsilon - \Lambda_0)$ might remain injective in the limit as $\varepsilon \to 0$. This distinguishes the case of thin tubular inclusions as considered here from the case of small point-like inclusions as considered, e.g., in [11], where the leading order term of the asymptotic expansion of the difference of the Neumann-to-Dirichlet operators has finite rank. Therefore, we use the Picard criterion (4.1) in our reconstruction method rather than the MUSIC algorithm, which is particularly adapted to the case of finite dimensional range spaces (cf. Cheney [16]). However, we mention that a MUSIC-type method in combination with a discretized model for the forward problem has recently been applied successfully to a similar problem in two dimensions by Park and Lesselier [40].

5.2. Numerical implementation of the reconstruction method. The Neumann function for the unit ball Ω can be computed explicitly (cf., e.g., Wloka [43, p. 361]) as

$$N(z,y) = \frac{1}{4\pi}\left(\frac{1}{|y-z|} + \frac{1}{\left|\frac{z}{|z|} - |z|y\right|} + \log\left(\frac{2}{1 - y\cdot z + \left|\frac{z}{|z|} - |z|y\right|}\right)\right) - \frac{1}{2\pi},$$

$z \in \Omega$, $y \in \overline{\Omega}$, $z \neq y$. So, for any unit vector $d \in \mathbb{R}^3$, $z \in \Omega$, and $y \in \partial\Omega$, the test function $g_{z,d}$ from (4.4) is given by

$$g_{z,d} = d \cdot \frac{1}{4\pi}\left(2\frac{y-z}{|y-z|^3} + \frac{1}{1 - y\cdot z + |y-z|}\left(y + \frac{y-z}{|y-z|}\right)\right).$$

For arbitrary domains Ω and constant background conductivities γ_0, an efficient way to evaluate the function $g_{z,d}$ by means of Λ_0 has been pointed out by Hanke and Brühl [26], and a corresponding method for inhomogeneous background media has recently been considered by Egger et al. [21].

Employing the singular value decomposition of M from (5.2), the function $W(z,d)$ from (4.5) can be approximated by

$$W_h(z,d) := \sum_{i=0}^{N} \frac{|\widetilde{g_{z,d}} \cdot \tilde{v}_i|^2}{\tilde{\sigma}_i} \Big/ \sum_{i=0}^{N} |\widetilde{g_{z,d}} \cdot \tilde{v}_i|^2, \tag{5.3}$$

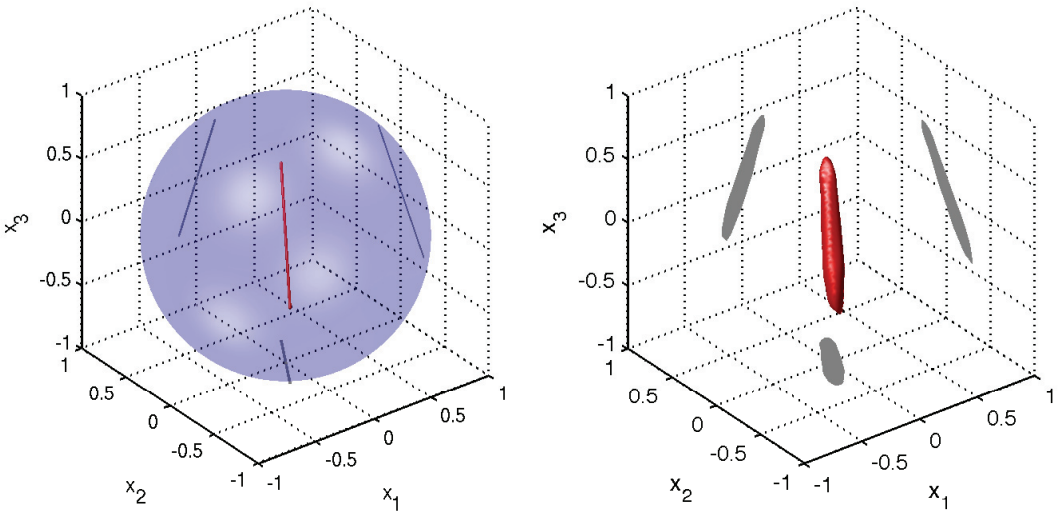

Figure 3. *Geometrical setup for Example 5.2 (left) and reconstruction (right).*

where $\widetilde{g_{z,d}}$ is the vector containing the coefficients of the expansion of $g_{z,d}$ in spherical harmonics Y_l^m, $-l \le m \le l$ and $1 \le l \le 8$. In our numerical examples below we use $N = 70$, i.e., much more singular values and singular vectors than are actually justified by the error bound (5.1). This improves the reconstructions, which has recently also been confirmed theoretically by Arens, Lechleiter, and Luke [5]. To fulfill (3.7), we compute $W_h(z, d)$ for three orthogonal test dipole polarizations $d = e_1$, $d = e_2$, and $d = e_3$, and combine the results for each test point $z \in \Omega_h$ to obtain the *indicator function*

$$\mathrm{Ind}(z) := \frac{1}{\log W_h(z, e_1)} + \frac{1}{\log W_h(z, e_2)} + \frac{1}{\log W_h(z, e_3)}.$$

This function should take its largest values close to the inclusion ω_ε. Hence, cross-sectional plots of Ind and plots of isosurfaces of Ind can be used to visualize the location of ω_ε.

Example 5.2 (reconstruction of a thin cylinder). We consider the straight cylindrical inclusion ω_ε with conductivity $\kappa = 0.5$ introduced in Example 5.1 with radius $\varepsilon = 0.01$. The simulated forward data for this example contain an estimated numerical error of 0.37%. The right-hand plot in Figure 3 shows the isosurface $\mathrm{Ind} = 0.85 \max_{z \in \Omega_h} \mathrm{Ind}(z)$ and its projections on the coordinate planes. Note that we do not attempt to reconstruct the actual radius of the inclusion ω_ε. Rather the isosurface is a three-dimensional visualization of possible locations of curves inside or close to ω_ε starting around $(-1/\sqrt{3}, -1/\sqrt{3}, -1/\sqrt{3})$ and ending around $(1/\sqrt{3}, 1/\sqrt{3}, 1/\sqrt{3})$.

The quality of this reconstruction is quite good. The length, position, and orientation of ω_ε can be well estimated. The smaller the isosurface is, i.e., the larger we choose the corresponding threshold, the better these estimates are. However, the threshold cannot be too large, as otherwise the isosurface degenerates or becomes the empty set. In this and the following examples we choose the thresholds by trial and error using the a priori information that there are few (possibly zero) thin tubular inclusions contained in Ω. As we will observe,

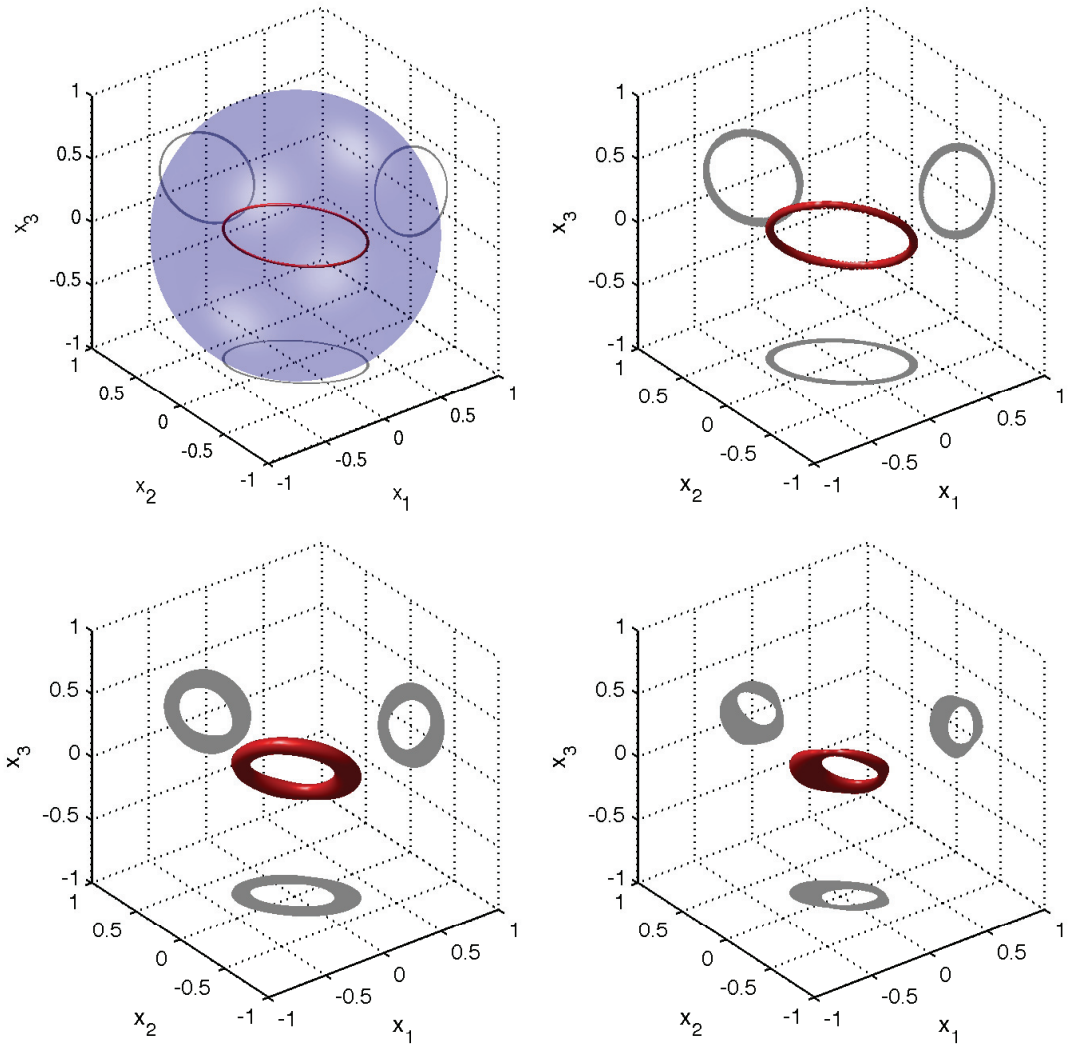

Figure 4. *Geometrical setup for Example 5.3 (top left), reconstruction without noise (top right), reconstruction with 1% noise (bottom left), and reconstruction with 3% noise (bottom right).*

the optimal threshold does not depend very much on the particular inclusion, but it increases with the amount of noise contained in the measurement data. We will also see that smaller isosurfaces can be obtained if the conductivity contrast is higher and if the inclusions are closer to the boundary of Ω.

Example 5.3 (reconstruction of a thin torus). In our second example for the reconstruction method the inclusion ω_ε is a thin torus centered at the origin such that the curve K in the center of its tube is a circle of radius 0.5, the radius of the tube itself is 0.01, and the axis of symmetry of the torus is aligned with the vector $(1,1,1)$ (see Figure 4 (top left) for a sketch of this setup). The conductivity inside ω_ε is given by $\kappa = 2$, and the simulated forward data for this example contain an estimated numerical error of 0.33%. The top right plot in Figure 4 shows the isosurface $\mathrm{Ind} = 0.85 \max_{z\in\Omega_h} \mathrm{Ind}(z)$ and its projections on the coordinate

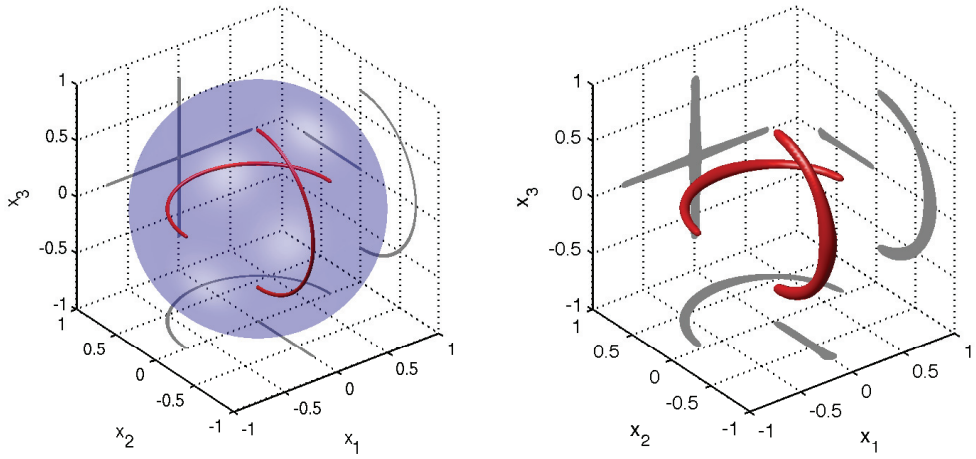

Figure 5. *Geometrical setup for Example 5.4 (left) and reconstruction (right).*

planes. The position and shape of the inclusion (not considering the radius of the tube) are well reconstructed.

In an attempt to study the effect of noise on our reconstruction method we add 1% (resp., 3%) uniformly distributed relative error to the simulated forward data and show the corresponding isosurface $\mathrm{Ind} = 0.98 \max_{z\in\Omega_h} \mathrm{Ind}(z)$ (resp., $\mathrm{Ind} = 0.99 \max_{z\in\Omega_h} \mathrm{Ind}(z)$) in Figure 4 (bottom row). With 1% noise the inclusion is still well reconstructed, while with 3% noise the isosurface starts to degenerate and the radius of the reconstructed object is too small. If we perturb the simulated forward data in this example by 5% uniformly distributed relative error, the reconstruction method still recovers a torus, but its radius is much too small. For higher amounts of noise the algorithm fails and reconstructs a single point-like object close to the center of mass of the inclusion ω_ε.

Example 5.4 (reconstruction of two thin arcs). Next, we consider an example for multiple inclusions as studied in the appendix. Two halves of a thin torus, $\omega_{\varepsilon,1}$ and $\omega_{\varepsilon,2}$, such that the distance from their center to the center of their tubes is 0.7 and the radius of their tubes itself is 0.015, are placed in the sphere Ω as shown in Figure 5 (left). The axis of symmetry of $\omega_{\varepsilon,1}$ and $\omega_{\varepsilon,2}$ is e_3 and e_1, respectively. We attach four small hemispheres of radius 0.015 to the ends of the tubes to avoid edges in the geometry. The conductivity inside the inclusions is given by $\gamma_1 \equiv \kappa_1 = 2$ in $\omega_{\varepsilon,1}$ and $\gamma_2 \equiv \kappa_2 = 3$ in $\omega_{\varepsilon,2}$, respectively. The simulated forward data for this example contain an estimated numerical error of 0.73%. The right-hand plot in Figure 4 shows the isosurface $\mathrm{Ind} = 0.85 \max_{z\in\Omega_h} \mathrm{Ind}(z)$ and its projections on the coordinate planes. The positions and the shapes of the two arcs are well reconstructed. Due to the different conductivities in $\omega_{\varepsilon,1}$ and $\omega_{\varepsilon,2}$, the values of the local maxima of Ind along the two inclusions are slightly different, and therefore the isosurface around the arc $\omega_{\varepsilon,1}$ is smaller than the isosurface around the arc $\omega_{\varepsilon,2}$.

This can also be observed in Figure 6, which shows cross-sectional plots of $\mathrm{Ind}(z)$ perpendicular to e_1 at $z_1 = -0.5$, $z_1 = 0$, $z_1 = 0.5$ (first row); perpendicular to e_2 at $z_2 = -0.5$, $z_2 = 0$, $z_2 = 0.5$ (second row); and perpendicular to e_3 at $z_3 = -0.5$, $z_3 = 0$, $z_3 = 0.5$ (third row). In accordance with Proposition 3.2 the indicator function Ind takes its largest values

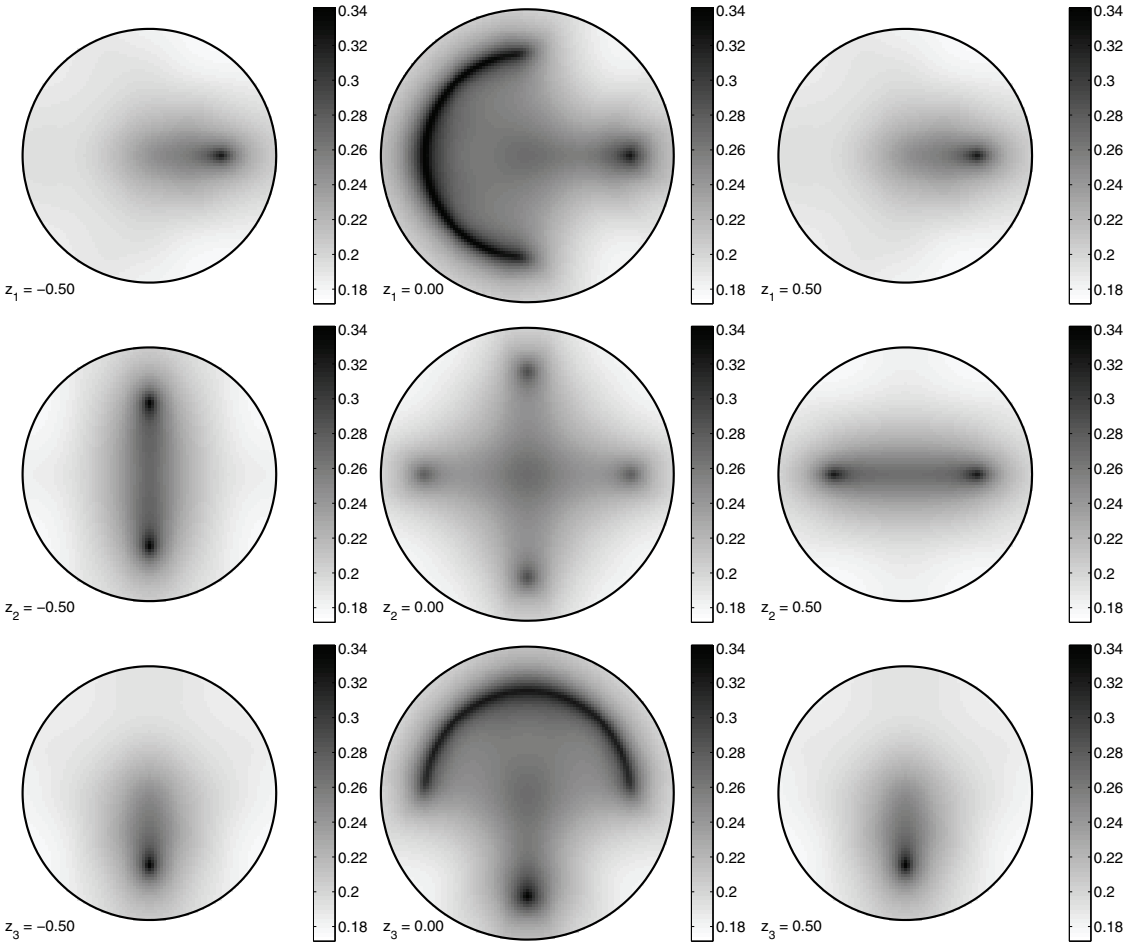

Figure 6. *Cross-sectional plots of* $\mathrm{Ind}(z)$ *at* $z_1 = -0.5$, $z_1 = 0$, $z_1 = 0.5$ *(first row);* $z_2 = -0.5$, $z_2 = 0$, $z_2 = 0.5$ *(second row); and* $z_3 = -0.5$, $z_3 = 0$, $z_3 = 0.5$ *(third row).*

close to the inclusions $\omega_{\varepsilon,1}$ and $\omega_{\varepsilon,2}$. The local maximum around $\omega_{\varepsilon,1}$ (bottom row, middle) is less pronounced than the local maximum around $\omega_{\varepsilon,2}$ (top row, middle). Away from the inclusions the values of Ind are smaller, although there are some artifacts inside the convex hull of the arcs. This phenomenon is well known from factorization and linear sampling methods for extended (i.e., nonthin) nonconvex inclusions (see, e.g., [26]).

Example 5.5 (reconstruction of a wire). In our final example we consider a highly conducting, rather irregularly shaped thin tubular object as shown in Figure 7. The radius of this tube is 0.01, the conductivity inside is given by $\kappa = 1000$, and the forward data for this example contain an estimated numerical error of 0.15%. The right-hand plot in Figure 7 shows the isosurface $\mathrm{Ind} = 0.88 \max_{z\in\Omega_h} \mathrm{Ind}(z)$ and its projections on the coordinate planes. Although the algorithm recovers the approximate position and orientation of the inclusion, the actual shape is very difficult to reconstruct due to its nonconvexity and because it is close to the center of Ω, i.e., far away from its boundary. We mention that the reconstructions get worse if we decrease the conductivity inside the object or add additional noise to the forward data.

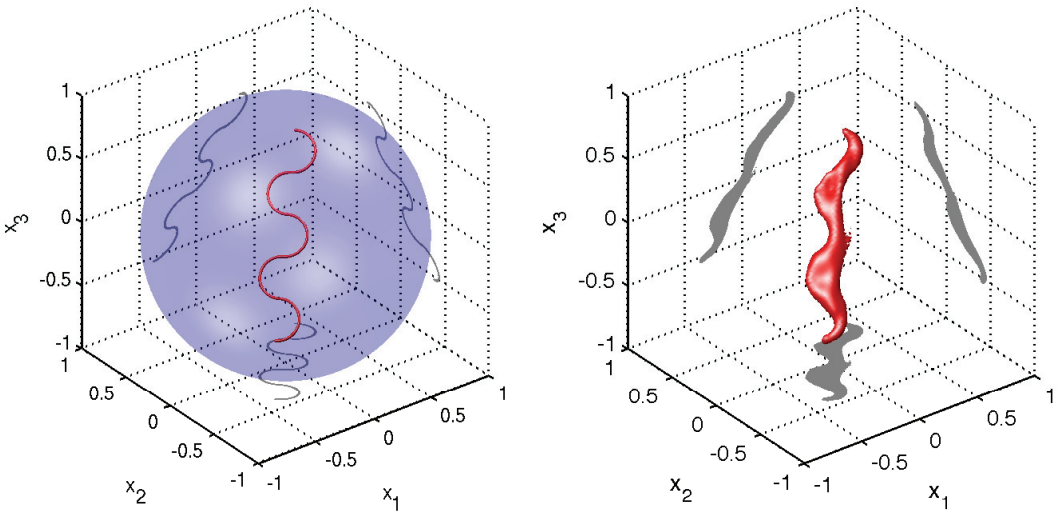

Figure 7. *Geometrical setup for Example 5.5 (left) and reconstruction (right).*

Conclusions. Our theoretical results show that the factorization method can be used to reconstruct infinitesimally thin tubular inclusions in some three-dimensional bounded domain from the leading order term in the asymptotic expansion of the difference of the Neumann-to-Dirichlet operators with and without inclusions.

Applying perturbation theory for linear operators, we used this result to establish a numerical algorithm to reconstruct thin tubular inclusions of finite thickness from finite dimensional realizations of the difference of the Neumann-to-Dirichlet operators $\Lambda_\varepsilon - \Lambda_0$. We have seen in our numerical results that this reconstruction method works remarkably well for simulated forward data and that it can handle a moderate amount of noise contained in these data.

As for every reconstruction method for inclusions of small volume, the applicability of our algorithm in practice will ultimately depend on the accuracy with which the boundary potential can be measured, since such inclusions have very little effect on the boundary potential.

Appendix. Multiple inclusions. In this section we generalize our results to the practically important case of finitely many well-separated thin tubular inclusions. By this we understand a collection of domains $\omega_{\varepsilon,1}, \ldots, \omega_{\varepsilon,m}$ of small volume such that

$$\omega_{\varepsilon,i} := \{(x, \varepsilon v) \in E_{K_i,r} \mid x + v \in B_i\},$$

$1 \leq i \leq m$, where $K_i \subset \Omega$ is a simple C^3 curve such that

$$\operatorname{dist}(K_i, \partial\Omega) \geq 2d_0 \qquad \text{and} \qquad \operatorname{dist}(K_i, K_j) \geq 3d_0 \quad \text{if } i \neq j,\ 1 \leq j \leq m,$$

for some positive constant d_0, E_{K_i} denotes the normal bundle of K_i in $\mathbb{R}^3$, $R(K_i)$ is the corresponding injectivity radius, and $B_i \subset U_{K_i,r}$ is a bounded domain contained in the tubular neighborhood $U_{K_i,r}$ of K_i, $r < R(K_i)$, such that B_i is a neighborhood of K_i without its

endpoints satisfying

$$\operatorname{dist}(B_i, \partial\Omega) \geq d_0 \qquad \text{and} \qquad \operatorname{dist}(B_i, B_j) \geq d_0 \quad \text{if } i \neq j,\ 1 \leq j \leq m.$$

Denoting by $\omega_\varepsilon := \bigcup_{i=1}^m \omega_{\varepsilon,i}$ the union of all inclusions, we consider a conductivity distribution

$$\gamma_\varepsilon(x) := \begin{cases} \gamma_i(x), & x \in \omega_{\varepsilon,i},\ 1 \leq i \leq m, \\ \gamma_0(x), & x \in \Omega \setminus \overline{\omega_\varepsilon}, \end{cases}$$

where $\gamma_i \in C^\infty(\Omega)$ is such that $0 < c_i \leq \gamma_i \leq C_i < \infty$ in Ω for some constants c_i and C_i and on each curve K_i the conductivity $\gamma_\varepsilon|_{K_i}$ is significantly smaller or larger than the background conductivity $\gamma_0|_{K_i}$ (the same for all curves).

Following section 2, we consider a sequence $(\varepsilon_n)_{n\in\mathbb{N}}$ in $]0,1]$ converging to zero, define functions $h_{0,i} \in L^\infty(K_i)$ as in (2.6), and extract a subsequence, also referred to as $(\varepsilon_n)_{n\in\mathbb{N}}$, such that for any boundary current $f \in L^2_\diamond(\partial\Omega)$ the solutions u_0 and u_{ε_n} of (2.1) and (2.5), respectively, fulfill

$$(u_{\varepsilon_n} - u_0)(y) = {\varepsilon_n}^2 \sum_{i=1}^m \int_{K_i} (\gamma_0 - \gamma_i)(x) \nabla_x N(x,y) \cdot \mathbb{M}(x) \nabla u_0(x) h_{0,i}(x)\ \mathrm{d}s(x) + o({\varepsilon_n}^2)$$

for $y \in \partial\Omega$, where $\mathbb{M}$ denotes the polarization tensor for $(\omega_{\varepsilon_n})_{n\in\mathbb{N}}$ (cf. [13]).

Introducing the operator $T : L^2_\diamond(\partial\Omega) \to L^2_\diamond(\partial\Omega)$,

$$Tf := \sum_{i=1}^m \int_{K_i} (\gamma_0 - \gamma_i)(x) \nabla_x N(x, \cdot\,) \cdot \mathbb{M}(x) \nabla u_0(x) h_{0,i}(x)\ \mathrm{d}s(x),$$

describing the leading order term in the corresponding asymptotic expansion of the difference of the Neumann-to-Dirichlet operators $\Lambda_{\varepsilon_n} - \Lambda_0$ similar to (3.1), the factorization from (3.6) remains true with $L : L^2(K_1;\mathbb{R}^3) \times \cdots \times L^2(K_m;\mathbb{R}^3) \to L^2_\diamond(\partial\Omega)$,

$$L(\psi_1, \ldots, \psi_m) := \sum_{i=1}^m \int_{K_i} \psi_i(x) \cdot \nabla_x N(x, \cdot)\ \mathrm{d}s(x),$$

and $F : L^2(K_1;\mathbb{R}^3) \times \cdots \times L^2(K_m;\mathbb{R}^3) \to L^2(K_1;\mathbb{R}^3) \times \cdots \times L^2(K_m;\mathbb{R}^3)$,

$$F(\phi_1, \ldots, \phi_m) := \left((\gamma_0 - \gamma_1) h_{0,1} \mathbb{M}|_{K_1} \phi_1, \ldots, (\gamma_0 - \gamma_m) h_{0,m} \mathbb{M}|_{K_m} \phi_m\right).$$

Since we assumed that either $\gamma_i|_{K_i} < \gamma_0|_{K_i}$ for all $i = 1, \ldots, m$ or $\gamma_i|_{K_i} > \gamma_0|_{K_i}$ for all $i = 1, \ldots, m$, accordingly either F or $-F$ is coercive. Therefore, Lemma 3.1(b) remains true, and the range characterization from Proposition 3.2 can be generalized as follows.

Corollary A.1. *Let $\Sigma \subset \Omega$ be a simple C^3 curve, let $\varphi \in C^1(\Sigma;\mathbb{R}^3)$ satisfying (3.7), and let $g_{\Sigma,\varphi} \in L^2(\partial\Omega)$ as in (4.4). Then, $g_{\Sigma,\varphi} \in \mathcal{R}(|T|^{1/2})$ if and only if $\Sigma \subset \bigcup_{i=1}^m K_i$.*

The reconstruction algorithm and its implementation in the case of multiple inclusions are the same as that described for a single inclusion in sections 4 and 5. In fact, the algorithm does not use any a priori information on the number of inclusions. Numerical results have already been shown in Example 5.4.

Acknowledgments. We are grateful to Fioralba Cakoni, David Colton, Peter Monk, and Michael Vogelius for inspiring and encouraging discussions in the course of this project. Furthermore, we thank Markus Brunk and Bastian Harrach for their help with FEMLAB.

REFERENCES

[1] H. Ammari, E. Beretta, and E. Francini, *Reconstruction of thin conductivity imperfections*, Appl. Anal., 83 (2004), pp. 63–76.
[2] H. Ammari, E. Beretta, and E. Francini, *Reconstruction of thin conductivity imperfections.* II. *The case of multiple segments*, Appl. Anal., 85 (2006), pp. 87–105.
[3] H. Ammari, R. Griesmaier, and M. Hanke, *Identification of small inhomogeneities: Asymptotic factorization*, Math. Comp., 76 (2007), pp. 1425–1448.
[4] H. Ammari and H. Kang, *Polarization and Moment Tensors with Applications to Inverse Problems and Effective Medium Theory*, Appl. Math. Sci. 162, Springer-Verlag, Berlin, 2007.
[5] T. Arens, A. Lechleiter, and D. R. Luke, *MUSIC for extended scatterers as an instance of the factorization method*, SIAM J. Appl. Math., 70 (2009), pp. 1283–1304.
[6] E. Beretta, Y. Capdeboscq, F. de Gournay, and E. Francini, *Thin cylindrical conductivity inclusions in a 3-dimensional domain: A polarization tensor and unique determination from boundary data*, Invere Problems, 25 (2009), 065004.
[7] L. Borcea, *Electrical impedance tomography*, Inverse Problems, 18 (2002), pp. R99–R136.
[8] M. Brühl, *Explicit characterization of inclusions in electrical impedance tomography*, SIAM J. Math. Anal., 32 (2001), pp. 1327–1341.
[9] M. Brühl and M. Hanke, *Numerical implementation of two noniterative methods for locating inclusions by impedance tomography*, Inverse Problems, 16 (2000), pp. 1029–1042.
[10] M. Brühl, M. Hanke, and M. Pidcock, *Crack detection using electrostatic measurements*, M2AN Math. Model. Numer. Anal., 35 (2001), pp. 595–605.
[11] M. Brühl, M. Hanke, and M. S. Vogelius, *A direct impedance tomography algorithm for locating small inhomogeneities*, Numer. Math., 93 (2003), pp. 635–654.
[12] M. Brunk, *Implementierung eines Verfahrens für die Impedanztomographie in drei Raumdimensionen*, Diplomarbeit, Johannes Gutenberg–Universität Mainz, Mainz, Germany, 2004.
[13] Y. Capdeboscq and M. S. Vogelius, *A general representation formula for boundary voltage perturbations caused by internal conductivity inhomogeneities of low volume fraction*, M2AN Math. Model. Numer. Anal., 37 (2003), pp. 159–173.
[14] Y. Capdeboscq and M. S. Vogelius, *Optimal asymptotic estimates for the volume of internal inhomogeneities in terms of multiple boundary measurements*, M2AN Math. Model. Numer. Anal., 37 (2003), pp. 227–240.
[15] Y. Capdeboscq and M. S. Vogelius, *Pointwise polarization tensor bounds, and applications to voltage perturbations caused by thin inhomogeneities*, Asymptot. Anal., 50 (2006), pp. 175–204.
[16] M. Cheney, *The linear sampling method and the MUSIC algorithm*, Inverse Problems, 17 (2001), pp. 591–595.
[17] M. Cheney, D. Isaacson, and J. C. Newell, *Electrical impedance tomography*, SIAM Rev., 41 (1999), pp. 85–101.
[18] D. Colton and R. Kress, *Inverse Acoustic and Electromagnetic Scattering Theory*, Appl. Math. Sci. 93, Springer-Verlag, Berlin, 1998.
[19] G. Dassios and R. Kleinman, *Low Frequency Scattering*, Oxford Math. Monogr., Oxford University Press, New York, 2000.
[20] R. Dautray and J. L.-Lions, *Mathematical Analysis and Numerical Methods for Science and Technology. Vol.* 1. *Physical Origins and Classical Methods*, Springer-Verlag, Berlin, 1990.
[21] H. Egger, M. Hanke, C. Schneider, J. Schöberl, and S. Zaglmayr, *Adjoint-based sampling methods for electromagnetic scattering*, Inverse Problems, 26 (2010), 074006.
[22] A. Friedman and M. S. Vogelius, *Identification of small inhomogeneities of extreme conductivity by boundary measurements: A theorem on continuous dependence*, Arch. Rational Mech. Anal., 105 (1989), pp. 299–326.

[23] B. Gebauer, *The factorization method for real elliptic problems*, Z. Anal. Anwendungen, 25 (2006), pp. 81–102.
[24] B. Gebauer and N. Hyvönen, *Factorization method and irregular inclusions in electrical impedance tomography*, Inverse Problems, 23 (2007), pp. 2159–2170.
[25] R. Griesmaier, *Detection of Small Buried Objects: Asymptotic Factorization and MUSIC*, Dissertation, Johannes Gutenberg–Universität Mainz, Mainz, Germany, 2008; available online from http://nbn-resolving.de/urn/resolver.pl?urn=urn:nbn:de:hebis:77-16663.
[26] M. Hanke and M. Brühl, *Recent progress in electrical impedance tomography*, Inverse Problems, 19 (2003), pp. S65–S90.
[27] M. Hanke and B. Schappel, *The factorization method for electrical impedance tomography in the half-space*, SIAM J. Appl. Math., 68 (2008), pp. 907–924.
[28] B. Harrach and J. K. Seo, *Detecting inclusions in electrical impedance tomography without reference measurements*, SIAM J. Appl. Math., 69 (2009), pp. 1662–1681.
[29] N. Hyvönen, *Complete electrode model of electrical impedance tomography: Approximation properties and characterization of inclusions*, SIAM J. Appl. Math., 64 (2004), pp. 902–931.
[30] N. Hyvönen, H. Hakula, and S. Pursiainen, *Numerical implementation of the factorization method within the complete electrode model of electrical impedance tomography*, Inverse Probl. Imaging, 1 (2007), pp. 299–317.
[31] T. Kato, *Perturbation Theory for Linear Operators*, Grundlehren Math. Wiss. 132, Springer-Verlag, Berlin, 1966.
[32] A. Kirsch, *Characterization of the shape of a scattering obstacle using the spectral data of the far field operator*, Inverse Problems, 14 (1998), pp. 1489–1512.
[33] A. Kirsch and N. Grinberg, *The Factorization Method for Inverse Problems*, Oxford Lecture Ser. Math. Appl. 36, Oxford University Press, New York, 2008.
[34] A. Kirsch and S. Ritter, *A linear sampling method for inverse scattering from an open arc*, Inverse Problems, 16 (2000), pp. 89–105.
[35] R. Kress, *Linear Integral Equations*, Appl. Math. Sci. 82, Springer-Verlag, New York, 1999.
[36] A. Lechleiter, *A regularization technique for the factorization method*, Inverse Problems, 22 (2006), pp. 1605–1625.
[37] A. Lechleiter, N. Hyvönen, and H. Hakula, *The factorization method applied to the complete electrode model of impedance tomography*, SIAM J. Appl. Math., 68 (2008), pp. 1097–1121.
[38] H. Lee and W.-K. Park, *Location search algorithm of thin conductivity inclusions via boundary measurements*, in Mathematical Methods for Imaging and Inverse Problems, ESAIM Proc. 26, EDP Sciences, Les Ulis, France, 2009, pp. 217–229.
[39] R. A. Litherland, J. Simon, O. Durumeric, and E. Rawdon, *Thickness of knots*, Topology Appl., 91 (1999), pp. 233–244.
[40] W.-K. Park and D. Lesselier, *MUSIC-type imaging of a thin penetrable inclusion from its multi-static response matrix*, Inverse Problems, 25 (2009), 075002.
[41] S. Schmitt, *The factorization method for EIT in the case of mixed inclusions*, Inverse Problems, 25 (2009), 065012.
[42] M. Spivak, *A Comprehensive Introduction to Differential Geometry*, Vol. 1, 2nd ed., Publish or Perish, Wilmington, DE, 1979.
[43] J. Wloka, *Partial Differential Equations*, Cambridge University Press, Cambridge, UK, 1987.